Flow Turbulence Combust (2013) 91:519–539
DOI 10.1007/s10494-013-9488-2

A New Divergence Free Synthetic Eddy Method for the Reproduction of Inlet Flow Conditions for LES

R. Poletto · T. Craft · A. Revell

Received: 7 November 2012 / Accepted: 27 June 2013 / Published online: 11 July 2013

Abstract This paper describes a recent development of the Synthetic Eddy Method (SEM) proposed by Jarrin et al. (Int J Heat Fluid Flow 30(3):435–442, 2009) for generation of synthetic turbulence. The present scheme is designed to produce a divergence-free turbulence field that can reproduce almost all possible states of Reynolds stress anisotropy. This improved representation, when used to provide inlet conditions for an LES, leads to reduced near-inlet pressure fluctuations in the LES and to a reduced development length, both of which lead to lower computer resource requirements. An advantage of this method with respect to forcing approaches (which require an iterative approach) is the suitability for direct usage with embedded LES. Results for a turbulent channel flow are reported here and compared to those from the original SEM, and other direct approaches such as the VORTEX method of Sergent (2002) and the Synthesized Turbulence approach of Davidson and Billson (Int J Heat Fluid Flow 27(6):1028–1042, 2006), showing overall improved performance and a more accurate representation of turbulence structures immediately downstream of the inlet.

Keywords Synthetic turbulence · Synthetic Eddy method · SEM · Embedded LES

1 Introduction

Large Eddy Simulation (LES) is gaining evermore industrial relevance due to increased computational capabilities and the ability to provide information about

R. Poletto (✉) · T. Craft · A. Revell
School of Mechanical Aerospace and Civil Engineering, The University of Manchester, Manchester M13 9PL, UK
e-mail: ruggero.poletto@gmail.com

instantaneous fluctuations. Despite this, the definition of quality assurance measures required for industrial usage of LES remains a challenge [2]. In contrast to Reynolds Averaged Navier-Stokes (RANS) methods, LES may not obviously reach a grid independent solution and, arguably, the majority of practical LES studies can be considered to be 'post-diction' rather than prediction (which nevertheless provides a very useful tool for detailed flow analysis). For industrially relevant complex geometry in particular, the computational requirements for what one could describe as an 'academically sound' LES study remain considerably high by most standards. As such there exists a substantial motivation to reduce the burden of such requirements by limiting the deployment of LES to those flow regions where one absolutely needs it, and applying a robust RANS approach in remaining parts of the domain. Such a methodology has been assigned the label of 'Embedded LES'. In this framework two new problems are introduced; a method to move from RANS regions to LES and a second to return back from LES to RANS. The present paper deals with the former issue, where one must superimpose physically representative instantaneous turbulent fluctuations onto mean velocity profiles obtained by the RANS models at the interface of the two domains. An algorithm for such a 'synthetic' turbulence approach should have three main characteristics:

- It should require a minimal spatial development distance of the LES downstream of the interface, so that the dimensions of the LES region may be minimised.
- It should require minimal computational effort compared to the resolution of the flow equations, so that the bottleneck is not with this algorithm.
- It should demonstrate satisfactory performance for input data coming from a RANS models. Given that the RANS model will generally be employed only in regions where one would expect good performance, it is reasonable to expect fairly reliable and realistic input data from it.

The need to define velocity boundary conditions which comprise a spatial and temporal variation is one that has been addressed by a number of different methods over the years, many of which have been developed for specific applications with specific solution techniques. In the following, we provide an overview of the techniques most relevant to the current study, but it is not our objective to exhaustively review this topic in its entirety, and thus the interested reader is referred to Sagaut et al. [13] and Tabor and Baba-Ahmadi [16] for a more comprehensive review of the subject. The latter review splits approaches into two main categories: those which use a precursor simulation to generate boundary information for use in the target simulation, and those which use various algorithms to synthetically reproduce 'turbulence-like' behaviour. Here we examine methods exclusively within the second of these categories, and specifically for the application to turbulent incompressible flow computed using Large Eddy Simulation. Following Tabor and Baba-Ahmadi [16], one can further classify approaches within the synthetic category into four subcategories:

1. Methods which make use of Fourier techniques, such as Batten et al. [1] and Davidson and Billson [3];
2. Methods which use data obtained from experimental measurements to reconstruct turbulence via Proper Orthogonal Decomposition, along the lines of Druault et al. [5];
3. Methods involving digital filters such as Di Mare et al. [9];

4. Those, such as the present method, which are based on the Lagrangian treatment of vortices, which are transported within a virtual box (e.g. [7, 14]).

It is well known that simply imposing random fluctuations on top of a mean velocity field is insufficient, since a long development length is required before the flow reaches what might be considered to be a realistic turbulent state. Lund et al. [8] proposed an early improvement to synthetic turbulence, by imposing a space correlation between the fluctuations; despite some improvement, shortfalls were still apparent as explained in Glaze and Frankel [6]. A further development was introduced by Sergent [14], who used randomly generated concentrations of vorticity in the stream-wise direction to generate span-wise and wall-normal fluctuations. While this approach demonstrated significant improvement over the previous methods, it was essentially a two-dimensional method and suffered drawbacks from the requirement that stream-wise fluctuations were generated by an altogether separate equation, thereby being uncorrelated with the other components.

A different solution to the problem was suggested by Batten et al. [1] and Davidson and Billson [3] who imposed spectral distributions of the target fluctuations by a superposition of goniometric functions. In these approaches the spectral signature of the turbulence was essentially approximated by a modified von Kármán spectrum.

More recently, Jarrin et al. [7] put forward a different approach to the problem where fluctuations are imposed by eddies convected through a virtual volume. This method was based on a three-dimensional correlation of fluctuations with a predefined shape function, and demonstrated an improved downstream development compared to other formulations; although recovery distance in a plane channel flow remained of the order of 10 half-channel heights. Subsequent work by Pamis et al. [11] demonstrated a substantial improvement over the original SEM by incorporating a more detailed definition of the eddy shape-function. In particular, multiple zones were defined in the near-wall region and the structure in each was adjusted to match well-documented observations of vorticity in the turbulent boundary layer. While the benefits of this approach are clear, some re-adjustment might become necessary for other flows. A more recent adaptation of the SEM method by De Meut [4] examined the use of volume forcing applied in an overlapping region of the RANS and LES domains, in order to further decrease the development length downstream of the inlet.

One drawback of the above schemes is that the fluctuating velocity fields they produce are not generally divergence-free. Although the velocity is usually imposed on a 2D inlet plane surface there is, nevertheless, a three-dimensionality associated with it, as the synthetically generated eddies are convected across the inlet plane into the computational domain. The LES procedure will, of course, generate suitable pressure variations to ensure that the velocity field inside the domain is divergence-free. However, if the inlet velocity does not come from a divergence-free field this may result in rather large pressure fluctuations near the inlet, to bring about the required rapid velocity changes. If, on the other hand, the incoming velocity came from a divergence-free field then one might smaller pressure fluctuations and velocity corrections to be needed near the inlet, resulting in improved flow development and lower computing costs.

The primary aim of the present work is to extend the original SEM formulation such that it is capable of generating a fluctuating velocity field that is divergence-free,

whilst still being able to return any given Reynolds stress statistics. The methodology is described in Section 2, with some initial tests reported in Section 3. The application of the new scheme to a plane channel flow is described in Section 4, along with a comparison of its performance alongside various other schemes.

2 The New Divergence Free SEM

2.1 SEM methodology

The present DFSEM is based on the methodology described in Jarrin et al. [7] where synthetic eddies, each of which represents a set of velocity fluctuations, are convected through a box that entirely surrounds the inlet plane upon which a turbulent velocity field is required. These eddies, which are defined by their centre and a formulation for the velocity fluctuation distribution around it, are convected at each time step by the locally imposed mean velocity. Once they have traversed and exited the box they are regenerated at a random location on the box inlet plane. In general, the steps of the DFSEM algorithm are summarized as:

1. User selection of inlet surface Ω.
2. User definition of average velocity $\mathbf{u}(\mathbf{x})$, Reynolds stresses and turbulence length-scales $\sigma(\mathbf{x})$, for $\mathbf{x} \subset \Omega$ (see Section 2.3 for a definition of the eddy length-scales).
3. Eddy Bounding Box taken as: $\max\{\mathbf{x} + \sigma\}$, $\min\{\mathbf{x} - \sigma\}$ for $\mathbf{x} \subset \Omega$.
4. Definition of the number of eddies (see Section 3).
5. Assigning random positions $\mathbf{x}^k$ and intensities α^k to all the eddies.
6. Eddies being convected through the eddy box, by $\mathbf{x}^k = \mathbf{x}^k + \mathbf{U}_b * \Delta t$, where $\mathbf{U}_b = \int_\Omega \mathbf{u} ds / \int_\Omega ds$ is the bulk velocity calculated from the user imposed average velocity. Eddies that leave the Bounding Box are re-generated at the opposite surface.
7. $\mathbf{u}'(\mathbf{x})$ calculated (see Section 2.2) and superimposed to $\mathbf{u}$ to generate the inlet condition.
8. Repeat steps 6–7 for all the subsequent time steps.

The reader is referred to Jarrin et al. [7] for more details about the overall procedure. The following sections will mainly deal with the definition of a divergence free fluctuating velocity field (step 7), which is the main difference between the present approach and the original SEM.

2.2 Divergence-free condition

The SEM proposed in Jarrin et al. [7] defines velocity fluctuations according to the following:

$$u_i'(\mathbf{x}) = \frac{1}{\sqrt{N}} \sum_{k=1}^{N} a_{ij} \varepsilon_j^k f_\sigma^k \left(\frac{\mathbf{x} - \mathbf{x}^\mathbf{k}}{\sigma^k} \right) \tag{1}$$

where N is the number of eddies introduced into the SEM domain; $\mathbf{x}^k$ is the location of the centre of the kth eddy; σ^k is the turbulence length-scale calculated at the eddy centre; $f_\sigma(\mathbf{x})$ is a suitable shape function; ε_j^k are random numbers with zero average

and $\left\langle \varepsilon_j^k \varepsilon_j^k \right\rangle = 1$ which represent the eddy intensities, and a_{ij} are the Lund coefficients as defined in Lund et al. [8] and written as

$$a_{ij} = \begin{bmatrix} \sqrt{R_{11}} & 0 & 0 \\ \dfrac{R_{21}}{a_{11}} & \sqrt{R_{22} - a_{21}^2} & 0 \\ \dfrac{R_{31}}{a_{11}} & \dfrac{R_{32} - a_{22}a_{31}}{a_{22}} & \sqrt{R_{33} - a_{31}^2 - a_{32}^2} \end{bmatrix} \tag{2}$$

where R_{ij} are the elements of the Reynolds stress tensor. Although this formulation allows any desired Reynolds stress field to be prescribed (via the a_{ij} coefficients), the velocity field will not, in general, be divergence free.

One route to obtain a divergence free method is to apply the original SEM methodology to the vorticity field, which is then transformed back to the velocity field by taking the curl of it. In fact, vorticity and velocity fields are linked by the following:

$$\nabla \times \omega' = \nabla(\nabla \cdot \mathbf{u}') - \nabla^2 \mathbf{u}' \tag{3}$$

in which, because of the hypothesis of incompressible flow, the first term on the right hand side vanishes, leading to a Poisson equation for the velocity field. The solution of this Poisson equation, achieved here by using the Biot–Savart kernel, leads to the fluctuating velocity field expressed as:

$$\mathbf{u}'(\mathbf{x}) = \sqrt{\frac{1}{N}} \sum_{k=1}^{N} \frac{q_\sigma(|\mathbf{r}^k|)}{|\mathbf{r}^k|^3} \mathbf{r}^k \times \alpha^k \tag{4}$$

where $\mathbf{r}^k = \frac{\mathbf{x} - \mathbf{x}^k}{\sigma^k}$, $q_\sigma(|\mathbf{r}|^k)$ is a suitable shape function and α_i^k are random numbers with zero average which represent the eddy intensities.

At this point it is important to note that despite the similarities between Eqs. 1 and 4, i.e. both including a user defined shape function and a random level eddy intensity, the lack of Lund coefficients in the second formulation poses a significant problem. Their role in the original SEM was crucial in order to allow any given turbulence state to be generated, however, they cannot be re-introduced to Eq. 4 without forgoing the divergence free condition[1] The following section describes how the present scheme has been developed to overcome this problem.

2.3 Reproduction of turbulence anisotropy

In order to increase the turbulence anisotropy reproduction capabilities the present method employs the formulation of Eq. 4, but with an anisotropic length-scale, σ_i, employed in each of the coordinate directions x_i, and allows a different shape

[1]This was the origin of the anisotropy limitation described by the current authors in Poletto et al. [12].

function to be associated with each direction. However, such a form no longer automatically satisfies the divergence-free condition ensured by Eq. 4, and further constraints on the shape functions need to be considered in order to retain a divergence-free field. A convenient way of proceeding is to redefine the shape functions to be of the form $q_\sigma = q|\mathbf{r}^k|^3$ where q is a function which depends on the locations $\mathbf{x}$ and $\mathbf{x}^k$, and $\mathbf{r}^k$ differs slightly from its previous definition, as it now takes into account the length-scale anisotropy: $r^k_\beta = \frac{x_\beta - x^k_\beta}{\sigma^k_\beta}$. The new general formulation for the velocity fluctuations then becomes:

$$u'_\beta(\mathbf{x}) = \sqrt{\frac{1}{N}} \sum_{k=1}^{N} q_\beta \left(\mathbf{x}, \mathbf{x}^k, \sigma^k\right) \varepsilon_{\beta j l} r^k_j \alpha^k_l \tag{5}$$

In the above the cross product present in Eq. 4 has been rewritten using the index notation for tensors, where ε_{ijl} is the Levi–Civita symbol, and no summation is implied over Greek subscripts. As noted above, with the redefined shape functions, the form of Eq. 5 no longer automatically satisfies the divergence-free condition. However, on substituting it into the condition that $\nabla \cdot \mathbf{u}' = 0$, a sufficient condition for ensuring a divergence-free velocity field can be found as:

$$r^k_2 \frac{\partial q_1}{\partial x_1} = r^k_1 \frac{\partial q_2}{\partial x_2}, \qquad r^k_3 \frac{\partial q_2}{\partial x_2} = r^k_2 \frac{\partial q_3}{\partial x_3}, \qquad r^k_3 \frac{\partial q_1}{\partial x_1} = r^k_1 \frac{\partial q_3}{\partial x_3} \tag{6}$$

A simple analytical function for q_i that satisfies the above restrictions is:

$$q_i = \begin{cases} \sigma_i \left[1 - (d^k)^2\right], & \text{if } d^k < 1 \\ 0, & \text{elsewhere} \end{cases} \tag{7}$$

where $d^k = \sqrt{(r^k_j)^2}$.

The function q_i chosen above is continuous everywhere, but its derivative is not strictly defined for $d^k = 1$, where it is only possible to define a right or left sided derivative. The above formulation thus defines a divergence-free velocity field everywhere except at the eddy surface ($d^k = 1$), although this formal omission is not believed to result in serious problems. The expression for the velocity obtained by substituting Eq. 7 into Eq. 5 can be written as:

$$u'_\beta(\mathbf{x}) = \sqrt{\frac{1}{N}} \sum_{k=1}^{N} \sigma^k_\beta \left[1 - (d^k)^2\right] \varepsilon_{\beta j l} r^k_j \alpha^k_l \tag{8}$$

Time-averaging the product of Eq. 8 with itself leads to an expression for the Reynolds stresses, from which one can examine how the prescription of the length-scales, σ^k_i, and intensities, α^k_i, affect the stress anisotropy associated with the synthetically generated field given by Eq. 8:

$$\left\langle u'_\beta u'_\gamma \right\rangle = \frac{1}{N} \sum_{k=1}^{N} \sigma^k_\beta \sigma^k_\gamma \varepsilon_{\beta j l} \varepsilon_{\gamma m n} \left\langle \left\{ \left[1 - (d^k)^2\right]^2 r^k_j r^k_m \right\} \right\rangle \left\langle (\alpha^k_l)(\alpha^k_n) \right\rangle \tag{9}$$

On examining Eq. 9, it is clear that the eddies are independent of each other, and that their intensities are uncorrelated (so $\langle \alpha^k_l \alpha^k_m \rangle = 0$ for $l \neq m$); as such, the predicted shear stresses ($\langle u'_\beta u'_\gamma \rangle$ for $\beta \neq \gamma$) will be zero. In order to overcome this problem, fluctuations in the global coordinate system are computed via a standard

Table 1 Constant C_2 values used in the present work

Γ	1	$\sqrt{2}$	$\sqrt{3}$	$\sqrt{4}$	$\sqrt{5}$	$\sqrt{6}$	$\sqrt{7}$	$\sqrt{8}$
C_2	2.0	1.875	1.737	1.75	0.91	0.825	0.806	1.5

rotation transformation of the eddies generated in the local principal axes coordinate system (where the Reynolds stress tensor is diagonal):

$$u_i'^G(\mathbf{x}) = C_1 R_{im}^{P\to G} u_m'^P \tag{10}$$

where $R_{im}^{P\to G}$ is the rotation transformation matrix from the principal to the global coordinate system, $u_m'^P$ and $u_i'^G$ are the velocity fluctuations in the principal axes and global systems respectively, and C_1 is a normalization coefficient required in order to have $\langle u_i'^2 \rangle = 1$ when $\langle (\alpha_l^k)^2 \rangle = 1$:

$$C_1 = \frac{\sqrt{10 V_0} \sum_{i=1}^{3} \frac{\sigma_i}{3}}{\sqrt{N} \prod_{i=1}^{3} \sigma_i} \min\{\sigma_i\} \tag{11}$$

where V_0 is the eddy box volume.

For the normal stresses, the contribution from the kth eddy in Eq. 9 thus gives

$$\langle u_\beta' u_\beta' \rangle = 2 C_2 \sigma_\beta^2 \varepsilon_{\beta ln} \langle (\alpha_l^k)^2 \rangle \langle (\alpha_n^k)^2 \rangle \tag{12}$$

where all the terms not explicitly reported are represented by C_2. The remaining problem is to choose appropriate length-scales and eddy intensities to ensure the above will return the desired Reynolds stress statistics, over a wide range of stress

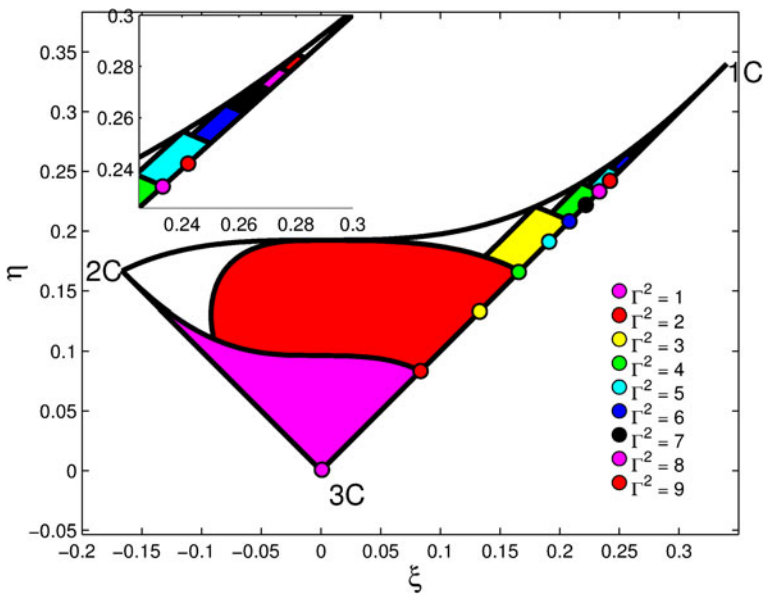

Fig. 1 Lumley triangle mapped with the new DFSEM. $6\eta^2 = b_{ii}^2$, $6\xi^3 = b_{ii}^3$ and $b_{ij} = \frac{\langle u_i' u_j' \rangle}{\langle u_k' u_k' \rangle} - \frac{1}{3}\delta_{ij}$. Mapped regions are defined by the values of Γ given in Table 1

anisotropy levels. It is found that for any choice of length-scale ratios (σ_x/σ_y and σ_x/σ_z), varying the intensity α_l^k allows one to reproduce possible turbulence anisotropy states over a particular region of the Lumley triangle. The approach taken has therefore been to define a series of ratios $\Gamma = \frac{\sigma_x}{\sigma_y} = \frac{\sigma_x}{\sigma_z}$ (effectively giving an elliptical shape to the eddies), as stated in Table 1, each allowing one of the regions of the triangle shown in Fig. 1 to be mapped. For a given Γ the Reynolds stresses are reproduced by defining the following intensities:

$$\left\langle (\alpha_\beta^k)^2 \right\rangle = \frac{\lambda_j/\sigma_j^2 - 2\lambda_\beta/\sigma_\beta^2}{2C_2} \tag{13}$$

where λ_i are the normal stresses in the local principal reference system. Since the right hand side of Eq. 13 must be positive, for any value of Γ it is only possible to reproduce a part of the triangle, and this is the reason for the sub-divisions shown in the Lumley triangle mapping. We note that for the set of Γ chosen in Table 1 most, but not quite all, of the Lumley triangle can be covered (for the test case considered in the present work, only structures appearing in the region $y^+ < 10$ are neglected). Indeed, the few remaining 'gaps' could easily be filled by selecting a larger set of ratios Γ.

3 Testing of the Isolated Eddy Box

The model, as defined in the previous section, was implemented and applied to an inlet surface of size $\delta \times \delta$ (with $\delta = 2 * \pi$), discretized by a grid of 128×128 nodes, imposing an isotropic state of turbulence and taking $U_b = 1$. A priori tests were conducted in order to assess the sensitivity of the method to some of the input parameters of the DFSEM, mainly the number of eddies required to achieve satisfactory levels of averaged statistics. In these cases no flow simulation is performed.

3.1 Assessment of the prescribed eddy density

Tests clearly demonstrate the impact of the factor $d = (\sigma_x \sigma_y \sigma_z N)/V_0$, which can be considered to represent the density of eddies imposed on the inlet plane. To illustrate this influence, results obtained for the streamwise velocity component u' at a particular spatial location are shown in Fig. 2 for low ($d = 0.1$), medium ($d = 1$) and high ($d = 10$) densities. The first plot displays the time trace of the instantaneous velocity u' as eddies pass through this location in the eddy box. Non-zero values indicate the influence of one or more eddies as they pass through. While signals with medium and high eddy density return a picture which is qualitatively 'turbulent' in nature, the low density case, $d = 0.1$, indicates a signal that appears to only pick up a single eddy at any given time, with frequent periods of zero activity indicating all eddies are beyond the immediate vicinity of the sampling point.

The second plot in Fig. 2 displays the computed values of the correlation $\langle u'u' \rangle$ as a function of the averaging time. As the computation progresses, this second moment should eventually return a value matching that of the imposed Reynolds stress. For the medium and high density cases, statistics are converged to within 10 % of the final value after only a few hundred time steps, while for the lower eddy density of $d = 0.1$ noticeably more time steps are necessary. This behaviour can be elucidated further

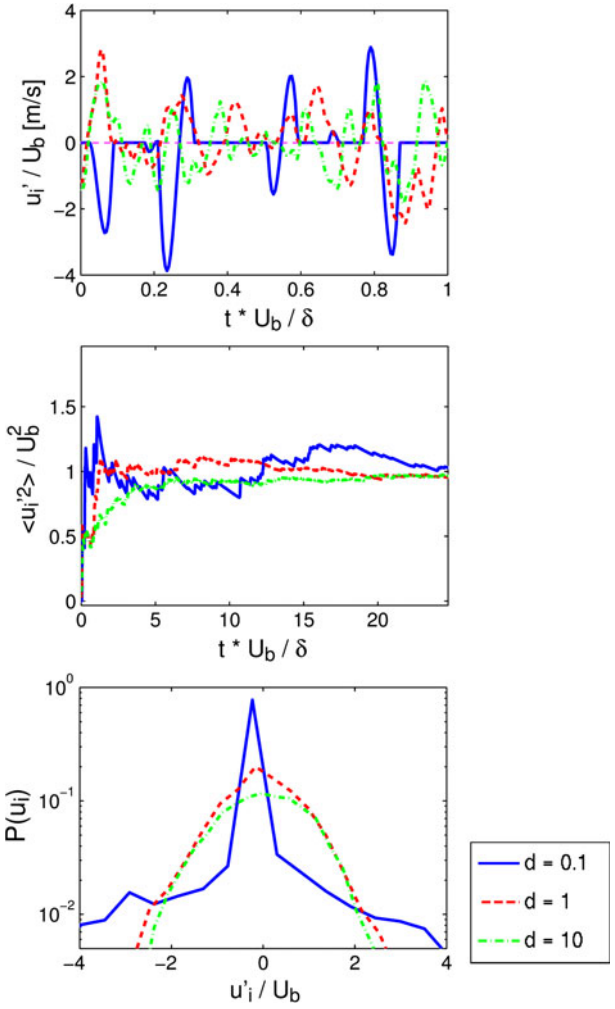

Fig. 2 Reproduction of an isotropic state of turbulence: influence of the eddy density d to the instantaneous velocity, to the convergence of $\langle u_i' u_i' \rangle$ and to the PDF

via a more detailed examination of the instantaneous synthetic turbulent velocity signal itself, and more specifically by plotting the associated Probability Density Function (PDF), as in the last plot of Fig. 2. As the eddy density is increased, a more complete PDF distribution is obtained.

Although the above results show the benefit of taking large values for d, the parameter is also significant from a computational standpoint, since the computational

Table 2 DFSEM CPU time for a single time step at various d (performed on a 2 MHz CPU)

d [adim]	0.06	0.77	1.00	5.91
CPU time [s]	0.035	0.176	0.220	1.288

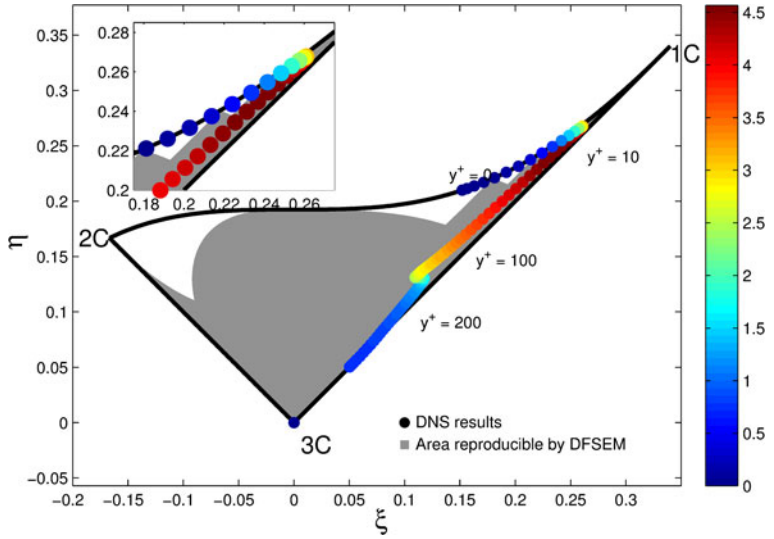

Fig. 3 Lumley triangle with data from Moser et al. [10] for a turbulent channel flow at ($Re_\tau = 395$), *coloured* by local turbulent kinetic energy. *Shaded areas* denote regions where DFSEM can capture the correct anisotropy

effort increases proportionally to the number of eddies in the box at any one time.[2] To demonstrate this point, the mean CPU time required per time step is provided for computations performed with a range of eddy densities in Table 2.

Since, for practical purposes, one would prefer the computational cost of a synthetic turbulence methodology to be negligible compared to the overall simulation cost, the above results suggest, somewhat logically, that a sensible compromise is to take an eddy density of d close to unity, which appears to give a good representation of the velocity PDF with a relatively fast simulation time.

3.2 Input data and length-scale definition

For the tests reported here the DNS data of Moser et al. [10] was used to provide Reynolds stress statistics for the DFSEM. These data are shown on the Lumley anisotropy triangle in Fig. 3, where the grey area denotes the states that can be fully reproduced by the method as described above in Section 2. As can be seen, most of the DNS data points do indeed lie in this grey area, implying that the DFSEM should be capable of returning stresses close to the desired levels. The few points lying outside the reproducible region are very close to the wall, mostly within the viscous sublayer, where turbulence levels are low, and the resultant errors in reproducing the turbulence anisotropy are not thought to be particularly serious.

Generally, in an Embedded LES framework, the Reynolds stresses for the DFSEM would come from a RANS model. Nevertheless, the present tests using full

[2] In particular the memory requirement for data storage becomes considerable for $d >> 1$.

DNS statistics seem to be most appropriate in order to demonstrate the performance of the DFSEM, and its capability to make full use of anisotropic Reynolds stresses. In fact, tests using data from a common RANS model, not reported here, have led to similar conclusions about the different inlet turbulence generation methods, and assessing the predictive accuracy of different RANS models is not the aim of the present work.

As described in Section 2.3, the present scheme permits Reynolds stress anisotropy whilst retaining a divergence-free velocity field via the prescription of *ratios* of the different length-scales σ_x, σ_y and σ_z, and their intensities $\langle(\alpha_i^k)^2\rangle$. The actual length-scale magnitude, here characterized by the average, $\sigma_{\text{avg}} = (\sigma_x + \sigma_y + \sigma_z)/3$, does not affect the Reynolds stress anisotropy in a homogeneous field, but does have some influence on the results in inhomogeneous situations, as will be seen below. In the present work the average length-scale, σ_{avg}, has been taken as

$$\sigma_{\text{avg}} = \min(k^{3/2}/\varepsilon, \kappa\delta, \max(\Delta x, \Delta y, \Delta z)) \tag{14}$$

where $k^{3/2}/\varepsilon$ is the local length-scale provided by the DNS data (or would come from the RANS model in a typical embedded LES application), δ is the channel half-height, and κ the Von-Karman constant. The resulting reconstructed Reynolds stress profiles generated by the DFSEM across the channel, compared to the DNS data, are shown in Fig. 4. The comparison is generally very satisfactory, with most of the stress anisotropy being captured and, furthermore, the correlation between u' and v' being accurately reproduced. There is, however, a slight overestimate of the near-wall peak $\langle u'u'\rangle$ value, and a careful examination also shows that the stresses returned by the DFSEM do not quite go to zero at the wall surface.

The reason for the discrepancies noted in Fig. 4 lies, at least partly, in the role of the length-scale prescription. Each eddy carries a certain set of velocity fluctuations across its entire volume, and its size, related to σ_{avg}, therefore determines the spatial extent over which these particular fluctuation levels are present as the eddy is convected across the inlet plane. In other words, the particular fluctuations associated with each eddy are seen not only on the trajectory of its centre, but also

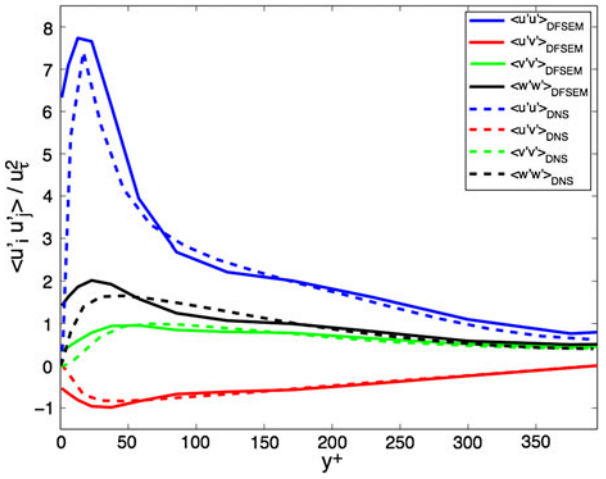

Fig. 4 Reproduced vs. prescribed profiles of Reynolds stresses

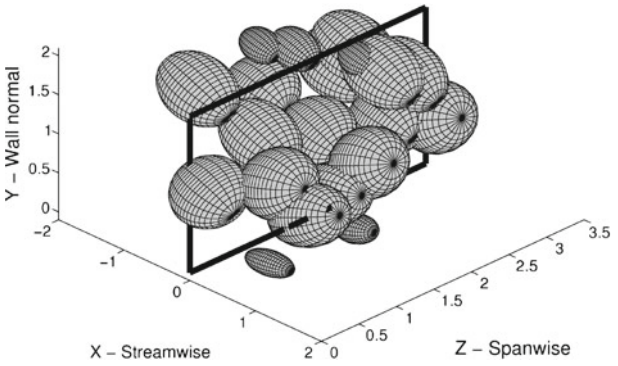

Fig. 5 Representation of the synthetic eddies convected across an inlet plane (*black rectangle*) by the DFSEM. Each *spheroid* represents the spatial region influenced by the perturbations from a single eddy

across a certain volume surrounding this point- determined by the size of the eddy. In order to visualize this behaviour, Fig. 5 provides a graphical representation of the eddies being convected through the inlet plane. The outlined rectangle indicates the location of the inlet surface and the ellipsoids are the eddies created by the DFSEM. As can be seen, the eddies are generally spherical towards the centre of the channel and elongated in the stream-wise direction as one approaches the wall. Different angles of inclination can also be seen, reflecting the changing direction of the Reynolds stress tensor principal axes. Each eddy carries velocity fluctuations which are applied across its whole volume, and hence contributes not only to the Reynolds stress levels on its centreline trajectory, but also to those in a certain area surrounding this. To characterise the effect of this *non-local* contribution of an eddy to the stress field, one can examine the quantity F, defined at point **P** by

$$F(\mathbf{P}) = \left| \frac{\partial \langle u_i' u_j' \rangle}{\partial y} \right| \cdot \frac{\sigma_{\text{avg}}}{u_\tau^2} \tag{15}$$

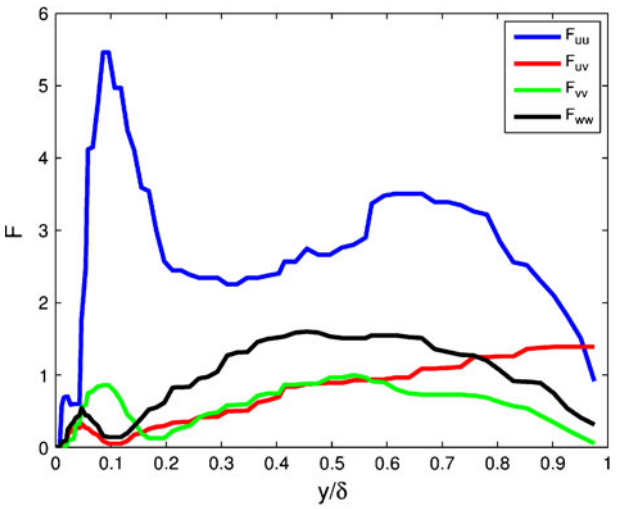

Fig. 6 Parameter F evaluated for the test case considered, channel flow $Re_\tau = 395$

This expression can be interpreted as a non-dimensional measure of the local spatial gradient of $\langle u_i' u_j' \rangle$, with respect to the local σ_{avg}. A high value implies that the locally prescribed length-scale will not be able to resolve fully the spatial variation of the Reynolds stresses. Figure 6 shows the variation of F across the channel in the present case, with length-scale σ_{avg} prescribed by Eq. 14. As would be expected from Fig. 4, the values of F associated with $\langle u'u' \rangle$ are highest, particularly close to the wall where $\langle u'u' \rangle$ changes value rapidly. Nevertheless, over most of the channel the values of F are below 4, and the resulting stress profiles in Fig. 4 suggest this is satisfactory.

4 Application to a Turbulent Channel Flow

4.1 Numerical setup

The new DFSEM, and other synthetic inlet methods, have been tested in generating inlet conditions for LES of a plane channel flow at $Re_\tau = 395$, for which reference DNS data is available from Moser et al. [10]. A domain of size $20\delta\pi \times 2\delta \times \pi\delta$ has been used (with $\delta = 1$), with inlet conditions applied via the various synthetic turbulence methods tested and standard Neumann boundary conditions applied at the outlet. The performance of the inlet methods can be most efficiently assessed by comparing the development of flow conditions downstream of the inlet, to examine how quickly they approach those of the fully developed channel flow. To allow this comparison, a fully periodic LES has also been performed with an identical mesh and numerical parameters.

The computations have been performed using *Code_Saturne*, on a mesh of $500 \times 46 \times 82$ cells, giving a total of 1.886.000 cells. These are arranged so that y^+ is around unity at the wall, and the non-dimensional grid-spacings in the stream-wise and span-wise directions are $\Delta x^+ = 50$ and $\Delta z^+ = 10$ respectively. A bulk velocity of $U_b/u_\tau = 17.55$ is imposed, via the inlet conditions, and the normalized time step used is $\Delta\tilde{t} = 0.07$ convective time units (CTUs), where the latter is defined as CTU $= \delta/U_b$. The Courant number was kept below one at all times. Second order accurate time and spatial discretizations have been employed, and the standard sub-grid scale model of Smagorinsky [15] was employed with a model constant of $C_s = 0.065$ (validated for *Code_Saturne*), along with classic near-wall damping following Van Driest [17]. The simulations have first been run for around 150 CTUs, after which statistics have been collected over a further 1500 CTUs.

4.2 Reducing the pressure fluctuations

When employing a method such as the original SEM, which does not produce a divergence-free incoming velocity field, one might expect there to be locally high pressure fluctuations around the inlet, associated with the LES enforcing a divergence-free condition in the first cell of the computation. However, in initial tests of the present channel flow this effect was masked by another feature present in both the SEM and DFSEM (and potentially in other schemes) when applied to bounded internal flows. This feature arises since stream-wise velocity fluctuations obtained

from the formulations described in Section 2 can result in a non-constant bulk flow rate into the channel. Although each individual complete eddy has zero mass flow, there will commonly be instances where only part of an eddy is inside the domain, and a numerical sampling of a finite number of them may then return a non-zero mass flow rate associated with the fluctuating field. This has the effect of inducing a time-dependent bulk flow rate, and consequently a time-dependent pressure drop along the channel.

To illustrate the impact of the above problem, Fig. 7 shows the levels of root mean squared (rms) pressure fluctuations along the channel for the original SEM of Jarrin et al. [7] and the DFSEM as described above (labelled as DF-SEM$_{nr}$ on the figure). In these calculations the fixed reference pressure is located at the channel exit, and consequently fluctuations in the bulk flow rate lead to fluctuations in pressure along the channel, and non-zero rms values, with the largest being at the inlet. Indeed, the DFSEM does produce lower rms values compared to the original SEM, but they are still quite significant and substantial. To address the above problem, a bulk correction was applied to the inlet velocity profile by simply introducing a rescaling coefficient to ensure the total mass flow rate across the inlet plane remained constant. The line labelled DFSEM in Fig. 7 shows the result of introducing this correction, and it can be seen that it almost entirely eliminates the corresponding pressure fluctuations.

Numerical simulations demonstrated that the above rescaling coefficient modified the velocity field by less than 1 % in the channel flow, and so its effect on the divergence-free feature of the scheme was deemed negligible. A further benefit of the correction was that it significantly reduced the required computational time for the simulations, since the large pressure fluctuations along most of the channel length entailed additional iterations on the pressure-velocity coupling. Finally, it is reiterated that the need for rescaling is likely to be restricted to the case of wall-bounded internal flows, in which small mass-imbalances lead to a more pronounced effect on the pressure field than they would for non-bounded flows.

Once the above scaling algorithm has been applied to the schemes, the impact of the divergence-free condition on local pressure fluctuations near the inlet can be

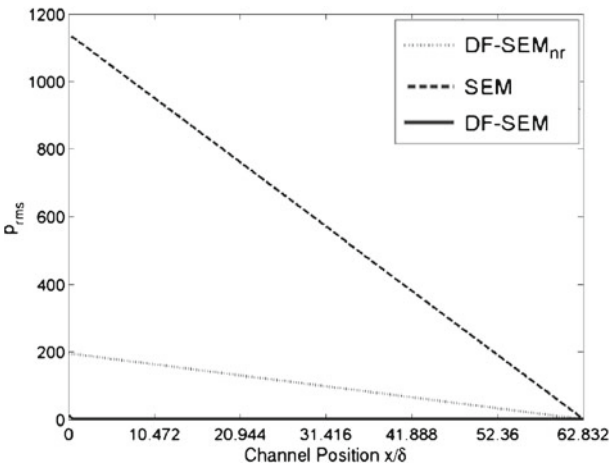

Fig. 7 Rms pressure fluctuations along the channel, using the original (unscaled) SEM and DFSEM (labelled as DFSEM$_{nr}$), and the DFSEM with velocity scaled to ensure a constant bulk flow rate

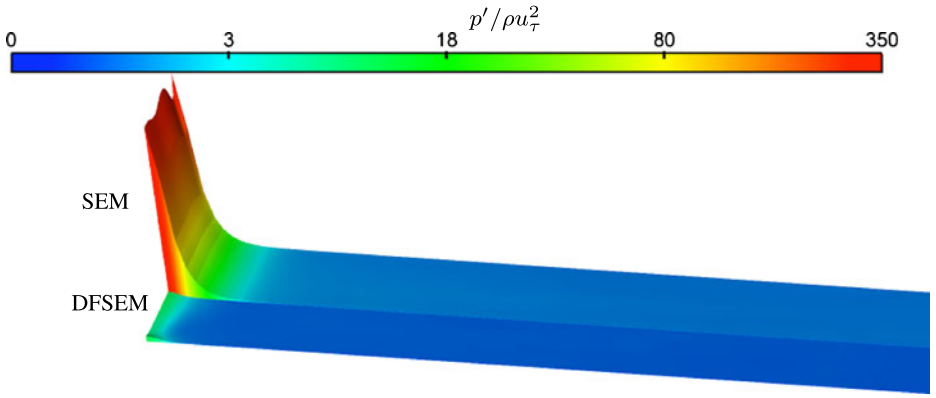

Fig. 8 RMS pressure fluctuations in the vicinity of the channel inlet with the SEM_{resc} and the DFSEM. Both simulations take advantage of the flow rescaling in order to minimize the pressure fluctuations along the channel

assessed more clearly. Figure 8 shows iso-surfaces of rms pressure fluctuation levels close to the inlet along the centre of the channel for both SEM_{resc} and DFSEM. As commented on above, in the simulations employing the SEM there are large pressure fluctuations immediately close to the inlet, where the LES has to impose a substantial correction to the incoming flow in order to obtain a divergence-free field in each computational cell. The DFSEM, on the other hand, results in much smaller fluctuations and a more uniform rms distribution across this region of the channel, since the abrupt changes to enforce continuity are no longer needed.

4.3 Benefit over the original SEM

Before undertaking a detailed comparison between the performance of several different schemes from recent literature, we first present some results to illustrate the incremental effect of the various elements that have been introduced into the DFSEM as described above. The objective is to provide insight into the relative benefit brought by each. As such we compare results from the following:

(i) The original SEM
(ii) SEM_{resc}: the original SEM with the mass rescaling described in Section 4.2
(iii) $\text{SEM}_{\text{any+resc}}$: the original SEM with both mass rescaling and anisotropic length-scales
(iv) DFSEM: taking the form described in the current paper.

Figure 9 shows the development of the wall skin-friction coefficient downstream of an inlet (located at $x/\delta = 0$) for all 4 of these methods. For reference, a periodic LES has been conducted on the same grid and the fully-developed value of C_f is plotted, together with lines indicating a 4 % deviation from this value. When synthetic turbulence is applied at a flow inlet, there is typically a sudden drop of the friction coefficient immediately downstream, before recovery to the fully-developed value occurs further downstream. The distance required for this coefficient to return to its fully-developed value is defined as the development length. The original SEM

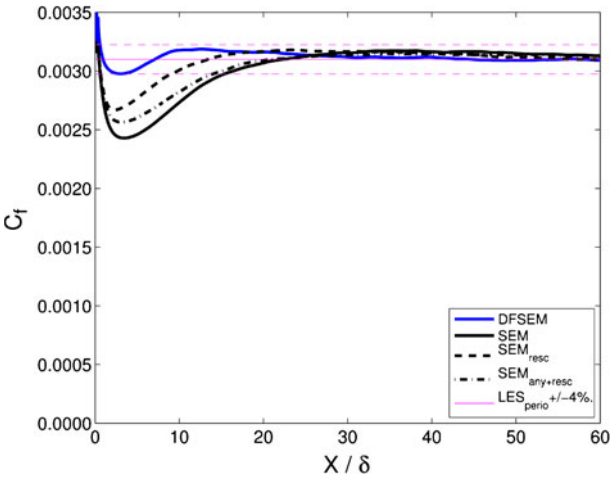

Fig. 9 Comparison of the C_f coefficient development with modified forms of the SEM and the final DFSEM

is seen to result in an initial drop in C_f of around 20 % before recovering to the fully developed value at $x/\delta \approx 20$. Introducing the mass-flow rescaling does result in an improvement, in terms of reducing both the magnitude of the initial dip in C_f and the development length.

To test the effect of introducing anisotropic length-scales, results from $\text{SEM}_{\text{any+resc}}$ employ a different length-scale in the three coordinate directions, linked to the prescribed normal stresses as $\sigma_{x_i} = \langle u_i u_i \rangle^{3/2}/\varepsilon$. Perhaps surprisingly the introduction of these anisotropic length-scales appears to worsen the scheme's performance. Nevertheless, employing these within the DFSEM scheme, in the manner described above that results in a divergence-free velocity field, can be seen to result in a significant improvement, with an initial drop of only around 4 % in C_f, and a rapid recovery.

4.4 Comparison of DFSEM with other proposed schemes

For a more detailed comparison between the DFSEM and other proposed schemes, the following section presents results obtained using the present DFSEM as described above, the original SEM of Jarrin et al. [7], the method of Sergent [14] (referred to as VORTEX) and the method of Davidson and Billson [3] (referred to as DB).

Figure 10 presents the development of the wall skin-friction coefficient. The DB and VORTEX schemes exhibit the most substantial drop-off from the inlet, both falling to around 55 % of the fully-developed value. The improvement brought by considering 3D eddies is clearly illustrated by the improved performance of the SEM and DFSEM, with the latter in particular producing only a very small initial drop, as noted above. In the case of these latter two approaches this short fall-off is followed by a small over-shoot before C_f slowly returns to the fully-developed value. In contrast, the VORTEX method predicts an evolution of C_f that returns more monotonically to the fully-developed value, although it only approaches this value much further downstream than the SEM and DFSEM schemes do, and does subsequently appear to drop slightly below the target value. The cause of the slight

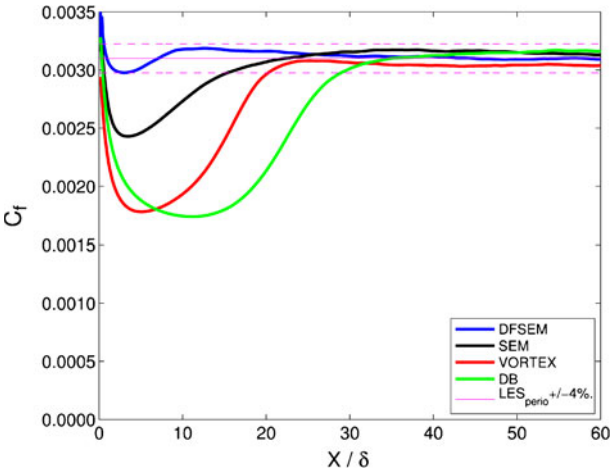

Fig. 10 C_f development along the channel; comparison of different inlet schemes against periodic solution. The DFSEM is compared against SEM, VORTEX and Davidson's (DB) methodologies

over-shoot of the velocity gradient in the case of the SEM and the DFSEM is yet to be fully identified, though one must point out the very near-wall nature of this quantity. Furthermore, in the context of an engineering model, it is very relevant to note that the DFSEM returns to a value within 4 % of the periodic solution after only a very short development distance, and remains within this bound throughout the rest of the domain.

A deeper insight into the structure of the resolved turbulent flow in the interior of the domain is gleaned from Figs. 11 and 12, by examining instantaneous values of vorticity. Contours of instantaneous ω_x are plotted at two planes parallel to the wall; Fig. 11 displays the plane $y/\delta = 0.05$ (close to the wall) while Fig. 12 displays

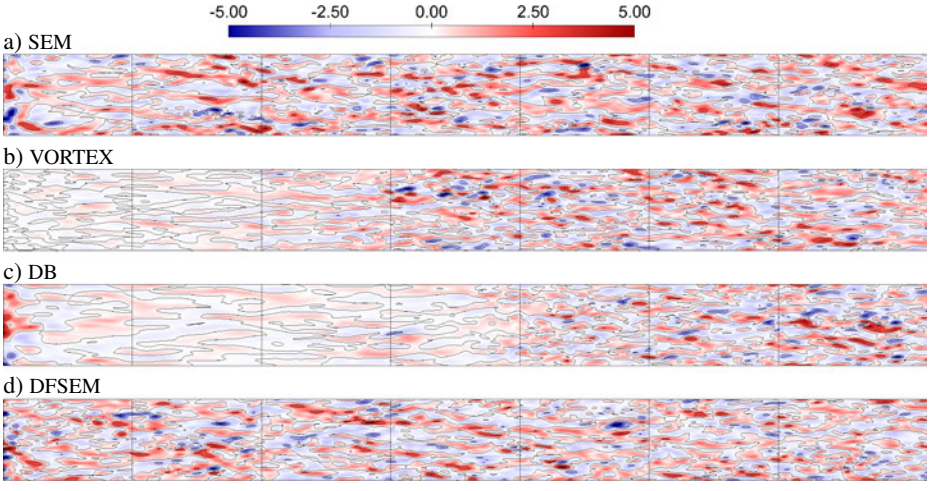

Fig. 11 Contours of stream-wise component of instantaneous vorticity, ω_x, over the XZ plane at $y/\delta = 0.05$. Flow left to right; where *vertical black lines* denote stream wise intervals of 5δ

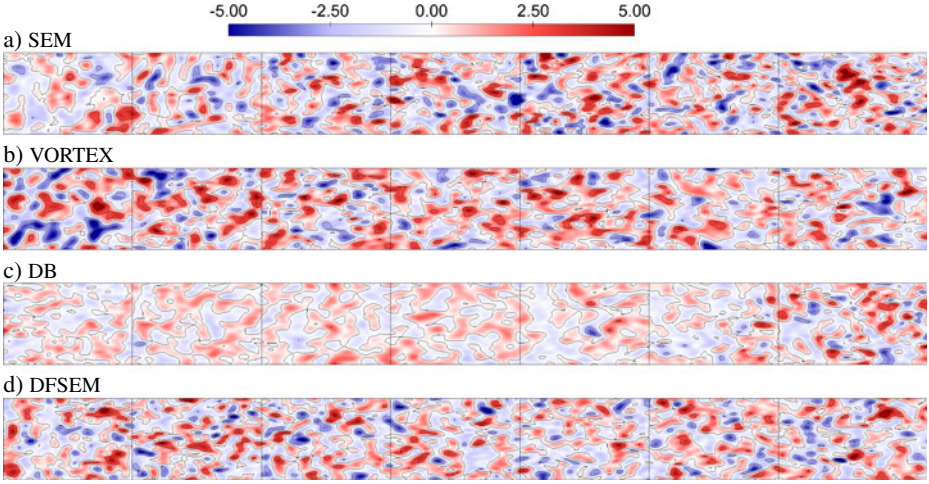

Fig. 12 Comparison of stream-wise component of instantaneous vorticity, ω_x, over the XZ planes at $y/\delta = 1$. Flow left to right; where *vertical black lines* denote stream wise intervals of 5δ

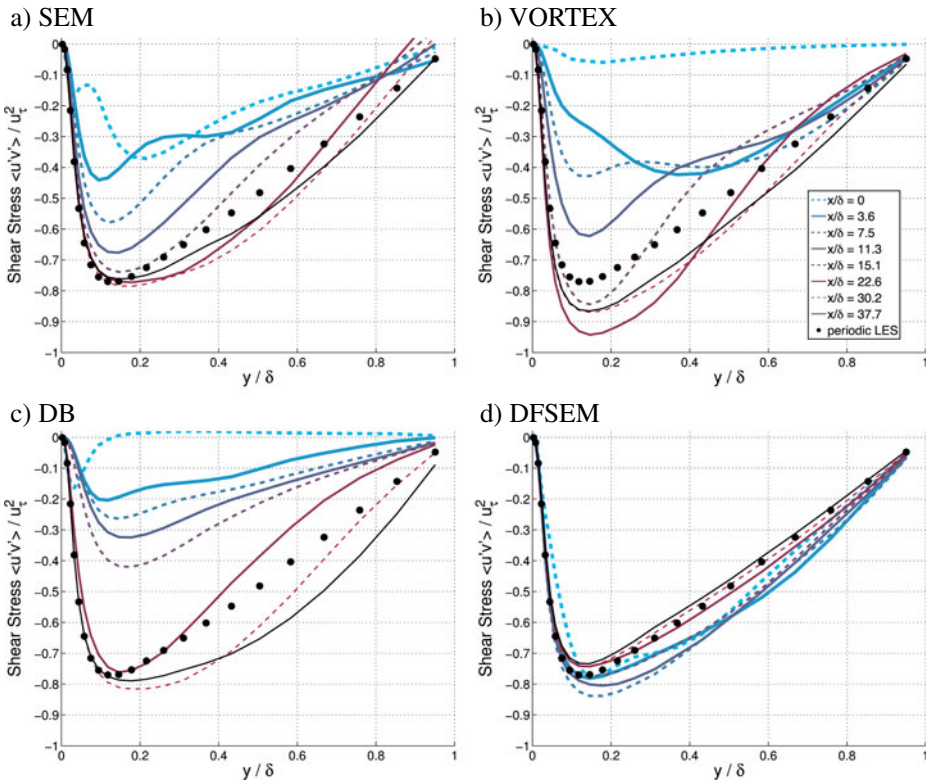

Fig. 13 $\langle u'v' \rangle$ profiles at selected stream-wise locations using various inlet conditions

the plane $y/\delta = 1$ (at the centre of the channel). In the near-wall region turbulence is known to develop into elongated stream-wise structures, which are clearly evident in the flow started with the SEM and DFSEM approaches in Fig. 11. The flow initiated by the VORTEX method indicates the correct qualitative behaviour, although the magnitude of the vorticity in this region is far lower than it should be, and does not deviate very much from zero within the region $x/\delta < 10$. The results from the DB approach indicate the presence of larger stream-wise structures, whose span-wise extent covers almost twice that of the correct dimensions, which are not recovered until around $x/\delta = 20$. Considering the flow near the channel centre, displayed in Fig. 12, one may draw largely similar conclusions, although the performance of the VORTEX method is noticeably improved. Indeed the more homogeneous, isotropic structure of turbulence in this region is perhaps more directly within the original philosophy of the VORTEX method. Attention is drawn to the ability of the DFSEM to simultaneously achieve an accurate representation of the turbulent structures in both near-wall and channel centre regions; testament to the ability of the scheme to reproduce turbulent fluctuation statistics across a range of Reynolds stress anisotropy levels.

In order to provide a more quantitative measure of the flow redevelopment, profiles of the Reynolds stress components have been extracted at selected locations

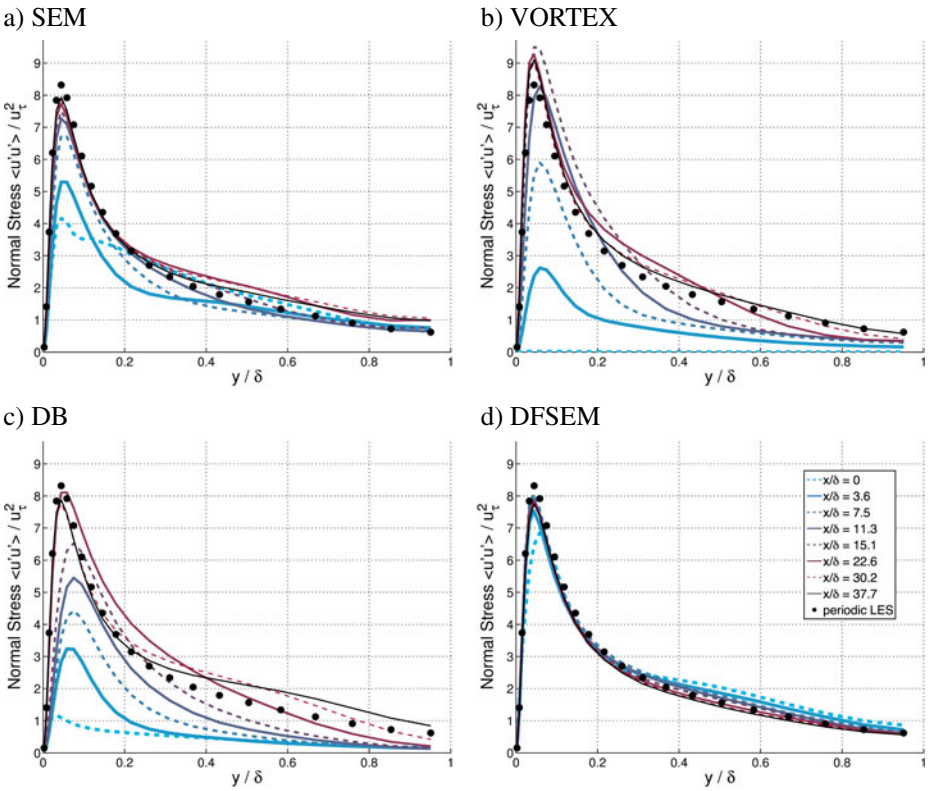

Fig. 14 $\langle u'u' \rangle$ profiles at selected stream-wise locations using various inlet conditions

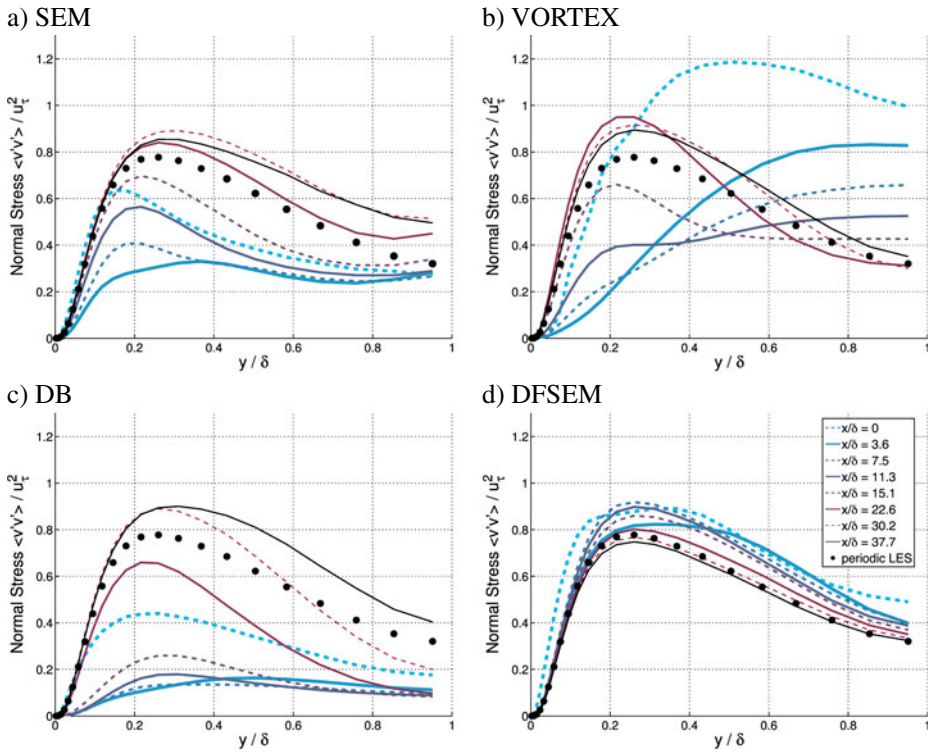

Fig. 15 $\langle v'v' \rangle$ profiles at selected stream-wise locations using various inlet conditions

downstream of the inlet and are presented in Figs. 13, 14 and 15. Figure 13 shows the shear stress development, from which it is clear to see that the original SEM results in a sudden drop of correlation between u' and v' after the inlet, associated with the reduction in turbulent structures and drop in C_f seen above. This drop does not appear in the new DFSEM case, and the profiles rapidly converge towards the fully-developed one. A similar picture emerges for $\langle v'v' \rangle$ and $\langle u'u' \rangle$ in Figs. 14 and 15. The initial reduction in $\langle v'v' \rangle$ associated with the SEM is perhaps not quite as severe as that seen in $\langle u'v' \rangle$. Nevertheless, because of the low level of turbulent correlations it still takes a significant distance to recover. The DFSEM approach again shows a much shorter recovery length, and for $\langle u'u' \rangle$ already returns very close to the fully-developed profile by $x/\delta \approx 3.6$.

5 Conclusions

A new synthetic turbulence generation method has been suggested as an improvement on the previous methodology of Jarrin et al. [7]. The new algorithm is able to impose a divergence free velocity field and to reproduce any possible state of Reynolds stress anisotropy as a function of the characteristic ellipsoid eddy shapes described by the aspect ratio Γ. Results from a turbulent channel flow have demonstrated a general decrease in the required development region downstream

of the inlet in a standard LES case: both the friction coefficient and the Reynolds stress profiles return to those obtained from a fully periodic computation in a shorter distance than that required by other methods tested.

The indicated reduced development length lead us to expect the method should result in significant computational savings when applied in fully embedded LES approaches, and further such tests are currently being carried out.

Acknowledgements The authors gratefully acknowledge support from EDF (Électricité de France) under contract 4200071890, and compute time from EPSRC on the UK National HPC Facility, HECToR. Part of this work was carried out under the EU project ATAAC (Advanced Turbulence Simulation for Aerodynamic Application Challenges) funded by the European Community in the 7th Framework Programme under Contract No. ACP8-GA-2009-233710-ATAAC.

References

1. Batten, P., Goldberg, U., Chakravarthy, S.: Interfacing statistical turbulence closures with large-eddy simulation. AIAA J. **42**(3), 485–492 (2004)
2. Celik, I.B., Cehreli, Z.N., Yavuz, I.: Index of resolution quality for large eddy simulations. In: Journal of Fluids Engineering, vol. 127. American Society of Mechanical Engineers, New York, NY, ETATS-UNIS (undefined Anglais) (2005)
3. Davidson, L., Billson, M.: Hybrid LES-RANS using synthesized turbulent fluctuations for forcing in the interface region. Int. J. Heat Fluid Flow **27**(6), 1028–1042 (2006)
4. De Meut, B.D.L.: Modélisation des écoulements turbulents en rotation et en présence de transferts thermiques par approche hybride RANS/LES zonale. Ph.D. thesis, Ecole Nationale Supérieure de Mécanique et d'Aérotechnique-Poitiers (2012)
5. Druault, P., Lardeau, S., Bonnet, J.-P., Coiffet, F., Delville, J., Lamballais, E., Largeau, J.-F., Perret, L.: Generation of three-dimensional turbulent inlet conditions for large-eddy simulation. AIAA J. **42**(3), 447–456 (2004)
6. Glaze, D.J., Frankel, S.H.: Stochastic inlet conditions for large-eddy simulation of a fully turbulent jet. AIAA J. **41**(6), 1064–1073 (2003)
7. Jarrin, N., Prosser, R., Uribe, J.-C., Benhamadouche, S., Laurence, D.: Reconstruction of turbulent fluctuations for hybrid RANS/LES simulations using a synthetic-eddy method. Int. J. Heat Fluid Flow **30**(3), 435–442 (2009)
8. Lund, T.S., Wu, X., Squires, K.D.: Generation of turbulent inflow data for spatially-developing boundary layer simulations. J. Comput. Phys. **140**(2), 233–258 (1998)
9. di Mare, L., Klein, M., Jones, W.P., Janicka, J.: Synthetic turbulence inflow conditions for large-eddy simulation. Phys. Fluids **18**(2), 025107 (2006)
10. Moser, R.D., Kim, J., Mansour, N.N.: Direct numerical simulation of turbulent channel flow up to $\mathrm{Re}_\tau = 590$. Phys. Fluids **11**(4), 943–945 (1999)
11. Pamis, M., Weiss, P.-L., Garnier, E., Deck, S., Sagaut, P.: Generation of synthetic turbulent inflow data for large eddy simulation of spatially evolving wall-bounded flows. Phys. Fluids **21**(4), 045103 (2009)
12. Poletto, R., Revell, A., Craft, T., Jarrin, N.: Divergence free synthetic eddy method for embedded les inflow boundary conditions. In: Seventh International Symposium On Turbulence and Shear Flow Phenomena (TSFP-7), Ottawa (2011)
13. Sagaut, P., Deck, S., Terracol, M.: Multiscale and Multiresolution Approaches in Turbulence. Imperial College Press London. ISBN: 186094650X (2006)
14. Sergent, M.E.: Vers une methodologie de couplage entre la simulation des grande echelles et les modeles statistiques. Ph.D. thesis, Ecole Central de Lyon (2002)
15. Smagorinsky, J.: General circulation experiments with the primitive equations: I. The basic experiment*. Mon. Weather Rev. **91**(3), 99–164 (1963)
16. Tabor, G.R., Baba-Ahmadi, M.H.: Inlet conditions for large eddy simulation: a review. Comput. Fluids **39**(4), 553–567 (2010)
17. Van Driest, E.R.: On turbulent flow near a wall. J. Aerosol Sci. **23**(11), 1007–1011 (1956)